

Particle Acceleration and Radiative Cooling in High-Energy Astrophysical Plasmas

Luis Bala, Noel James, Aadish Joshi, Jai Mirchandani, Olaf Willocx

2023-2024

The logo of KU Leuven, featuring the text "KU LEUVEN" in white on a blue background, enclosed in a thin white border.

KU LEUVEN

KU Leuven
Introduction to Plasma Dynamics

Contents

1	Introduction	2
1.1	Data	2
1.2	Lorentz Force & Leapfrog	3
1.3	Radiative Cooling in Tristan	4
1.4	Electron Energy Distributions for High Energy Plasmas	5
2	Methodology	6
2.1	Particle-in-Cell (PIC) Simulations and Tristan	6
2.2	Some necessary Tristan specifics	6
2.3	Sampling	7
2.4	Boris Mover	7
2.5	Operator Splitting	8
2.6	Parallelization	8
3	Results	9
3.1	Particle Trajectories	9
3.2	Electron Energy Distribution	10
3.3	Steady State Distributions for Different Cooling Strengths	11
3.4	Transferred Power	15
4	Conclusion	18

Abstract

There are various factors that affect the acceleration and net kinetic energy of particles in a high energy plasma. In this project, we have used the operator splitting method to numerically integrate the motion of a particle in a 3D periodic turbulent box, and have taken into account the radiation forces such as synchrotron radiation and inverse Compton cooling, which lead to a decrease in the net acceleration of the particle. We have obtained the evolution of electron energy distributions for different cooling strengths to understand the radiation dynamics in a high energy plasma. Further, we have also obtained the pitch angle distributions for plasmas with different cooling strengths to understand their anisotropic nature.

1 Introduction

Astrophysical sources like X-ray binaries and black hole accretion disks are known to emit electromagnetic radiation of very high energy due to the presence of plasma processes like turbulence and magnetic reconnection. The electrons that are energized in this process accelerate to relativistic speeds, with correspondingly high kinetic energies. But during this particle acceleration process, some energy is lost due to radiative cooling, resulting in a reduction of the kinetic energy of the particle [1]. In this project, we have taken into account two such drag forces, namely synchrotron radiation and inverse Compton cooling. But, before diving into the forces that result in the retardation of particles, we will first look into the acceleration dynamics resulting from the high-energy plasma processes.

1.1 Data

We have a 160^3 size snapshot of a PIC code of a turbulent plasma. We were told the magnetic field \mathbf{B} is aligned along $\hat{\mathbf{z}}$. Indeed, Figure 1 shows two columns along $\hat{\mathbf{z}}$. (It looks like three but it's a periodic box.) We obtained this image by writing the custom HDF5 file as a standard VTK image file and rendering it in ParaView, with a colormap that removes small values of $|B_z|$.

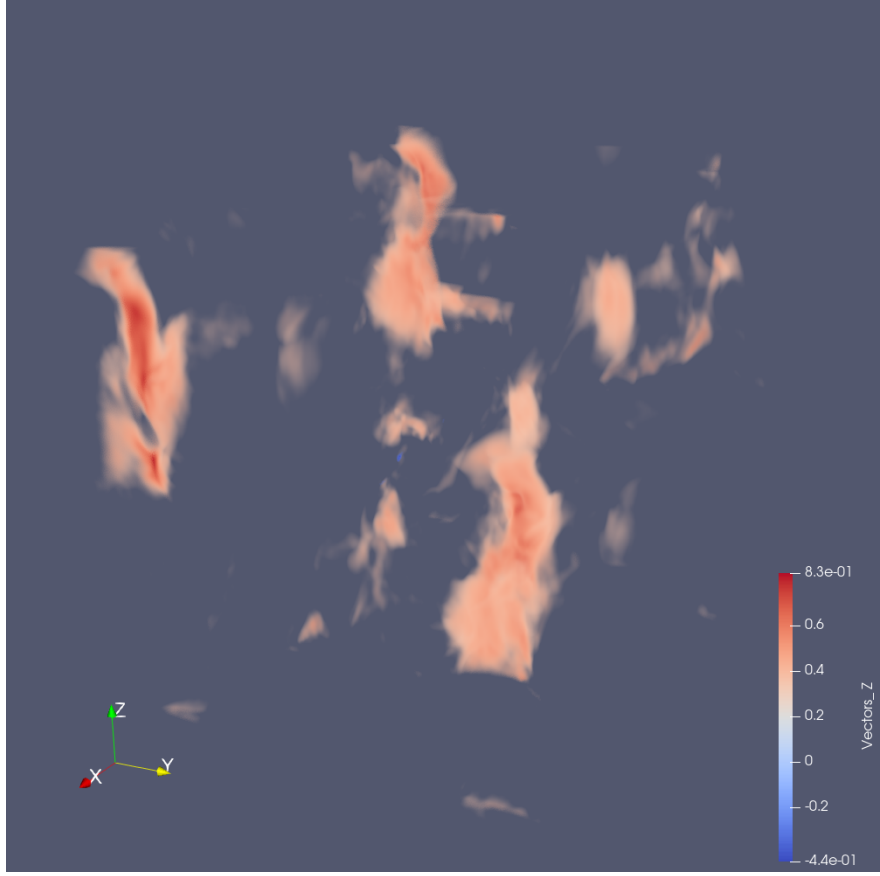


Figure 1: Two columns of \mathbf{B} along $\hat{\mathbf{z}}$

1.2 Lorentz Force & Leapfrog

The leapfrog integrator is 2nd order. It is a well known symplectic integrator. But symplectic integrators only work for symplectomorphic time evolution, i.e. conservative forces, so the leapfrog integrator applied to the Lorentz force in plasma dynamics is not symplectic. The Lorentz force contains a momentum term. This momentum should be a 2nd order accurate approximation to \mathbf{v}^n , as to keep the leapfrog integrator 2nd order accurate, i.e. it must be a centered mean:

$$\frac{d\mathbf{p}}{dt} = q(\mathbf{E} + \mathbf{v} \times \mathbf{B}) \quad (1)$$

$$\frac{\mathbf{p}^{n+1/2} - \mathbf{p}^{n-1/2}}{\Delta t} = q \left(\mathbf{E}^n + \frac{\mathbf{v}^{n+1/2} + \mathbf{v}^{n-1/2}}{2} \times \mathbf{B}^n \right) \quad (2)$$

This makes the leapfrog integrator implicit. However, it is semi-implicit, i.e. it can be rewritten explicitly. The exact way to do this is a bit complicated, but the Boris mover is the well known algorithm that is identical to this explicit reformulation. We will discuss the Boris mover in more detail in Section 2.3, because its implementation is more useful in a numerical context with undimensionalized quantities.

1.3 Radiative Cooling in Tristan

As relativistic plasma environments are often turbulent and hot in astrophysical systems such as accretion flows, relativistic jets, and active galactic nuclei, the effects of radiative cooling become significant [2]. Applying the phenomenon of radiative cooling in a plasma environment in the high-temperature, high-energy regime results in the production of several physical effects. Principally, as the radiative cooling thermalizes the plasma and regulates the temperature of the system towards equilibrium [3], we expect the effect to reduce the non-thermal electrons in the population by either steepening its distribution or introducing a high-energy cut-off [4]. Radiative cooling may also result in the overall thermalization of the Maxwell-Jüttner distribution of the system in the relativistic regime [5]. We will take a closer look at two types of cooling mechanisms responsible for regulating the acceleration dynamics of the particles in the plasma: inverse Compton cooling and synchrotron cooling.

The inverse Compton (IC) effect is a cooling mechanism for relativistic and thermal electrons applied in the context of particle dynamics in extreme astrophysical environments [6]. The effect normally considers a system where a low energy photon is scattered by a relativistic electron and generates a quasi-monochromatic, high-energy X-ray source [7]. In synchrotron cooling, the electrons are subjected to the effect by a turbulent magnetic field and cooled to some characteristic energy γ_{syn} during the period of emission [8]. Stronger synchrotron cooling leads to a notable compression of the plasma and the magnetic field, where radiative losses result in the decrease of plasma temperature and a delimiting of the nonthermal particle acceleration [9].

Using the mathematical prescriptions from the astro-plasma particle-in-cell code Tristan (v.2), we may write the synchrotron acceleration as

$$\frac{c \mathbf{d}\mathbf{u}}{dt} = \frac{|e|}{m_e} B_{\text{norm}} \frac{\beta_{\text{rec}}}{\gamma_{\text{syn}}^2} (\boldsymbol{\kappa}_R - \gamma^2 \chi_R^2 \boldsymbol{\beta}), \quad (3)$$

where $c\mathbf{u}$ is the spatial component of the 4-velocity of the electrons¹, e the electron charge, m_e the electron mass, B_{norm} a normalization factor for the electromagnetic fields ($\mathbf{E} = B_{\text{norm}}\mathbf{e}$ and $\mathbf{B} = B_{\text{norm}}\mathbf{b}$, \mathbf{e} and \mathbf{b} dimensionless), $\beta_{\text{rec}} = 0.1$ is a dimensionless quantity, the ‘fiducial magnetic energy extraction rate’, γ_{syn} is a characteristic Lorentz factor γ at which to heavily cool, and $\boldsymbol{\beta}$ is \mathbf{u}/γ . \mathbf{u} and $\boldsymbol{\beta}$ are both dimensionless. $\boldsymbol{\kappa}_R$ and χ_R^2 are dimensionless quantities describing how the electromagnetic fields cool the plasma through the Lorentz force:

$$\boldsymbol{\kappa}_R = (\mathbf{e} + \boldsymbol{\beta} \times \mathbf{b}) \times \mathbf{b} + (\boldsymbol{\beta} \cdot \mathbf{e}) \mathbf{e}, \quad (4)$$

$$\chi_R^2 = (\mathbf{e} + \boldsymbol{\beta} \times \mathbf{b})^2 - (\boldsymbol{\beta} \cdot \mathbf{e})^2. \quad (5)$$

The exact definition of γ_{syn} is that a particle with $\gamma = \gamma_{\text{syn}}$ in a (undimensionalized) magnetic field $\mathbf{b} = \mathbf{1}$ experiences a radiation force identical to the acceleration from an (undimensionalized) electric field $\mathbf{e} = \beta_{\text{rec}} \mathbf{1}$.

¹This is confusingly called the 4-velocity in literature. It is not a literal 4-velocity, nor is it a 3-velocity: it is the spatial component of the 4-velocity. The 4-velocity is the 4-momentum per mass, and so $c\mathbf{u}$ is the 3-momentum per mass.

Similarly, we have an acceleration due to inverse Compton cooling. Tristan assumes an isotropic soft radiation field, and a negligible Klein-Nishina effect. The acceleration is described by

$$\frac{cd\mathbf{u}}{dt} = -\frac{|e|}{m_e} B_{\text{norm}} \beta_{\text{rec}} \frac{\gamma^2}{\gamma_{\text{IC}}^2} \boldsymbol{\beta}, \quad (6)$$

where γ_{IC} , similar to γ_{syn} , is a characteristic Lorentz factor to start heavily cooling. The exact definition of γ_{IC} is that with a Thomson cross section σ_T and radiative energy density U_{ph} , the radiative force on a particle with $\gamma = \gamma_{\text{IC}}$, that is $-\frac{4}{3}\sigma_T U_{\text{ph}} \gamma_{\text{IC}}^2 \boldsymbol{\beta}$, is equated to the simple result $-|e|\beta_{\text{rec}} B_{\text{norm}} \boldsymbol{\beta}$. The effect for arbitrary γ is then a trivially re-scaled version of this, such is the idea.

1.4 Electron Energy Distributions for High Energy Plasmas

The distribution of the velocities of particles in a relativistic environment can be accurately modeled by the distribution scheme of Maxwell-Jüttner, which serves as the relativistic modification of the classical Maxwell-Boltzmann distribution scheme of particles. As gas particles in a plasma environment increase in temperature and the energy $k_B T$ approaches the relativistic limit mc^2 , the relativistic Maxwellian gas is described by the Maxwell-Jüttner distribution function,

$$f(\gamma) = \frac{\gamma^2 \beta(\gamma)}{\theta K_2(\frac{1}{\theta})} e^{-\gamma/\theta}, \quad (7)$$

where K_2 is the modified Bessel function of the second kind, $\theta = k_B T / mc^2$, and $\beta(\gamma) = v/c = \sqrt{1 - 1/\gamma^2}$.[10]

The distribution function assumes important consequences in the high-temperature regime existing in fusion plasmas and astrophysical plasmas observed in X-rays, in the context of high-energy astrophysics.[11] The probability distribution function (PDF) of the Maxwell-Jüttner distribution can be plotted as a function of the parameter γ :

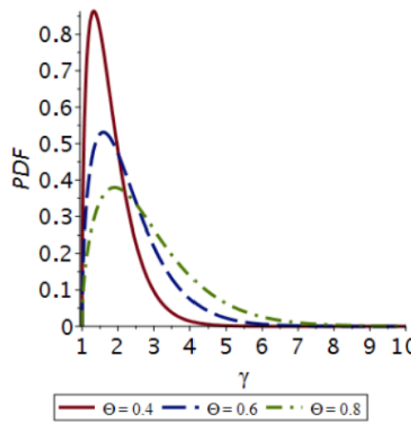


Figure 2: Probability distribution function of the Maxwell-Jüttner velocity distribution [12]

2 Methodology

2.1 Particle-in-Cell (PIC) Simulations and Tristan

In modelling the dynamics of a specific plasma environment, the underlying numerical algorithms rely on the computational framework of multi-dimensional grids using the so-called *particle-in-cell* or PIC approach, where the kinetic description of the environment is governed by sampling the distribution function with superparticles and representing the electromagnetic field in a grid [13]. In particular, the astro-plasma particle-in-cell framework Tri-dimensional Stanford Code (Tristan v.2) was utilized in modelling our assigned high-energy turbulent plasma.

Multi-dimensional particle codes typically assume a high computational demand, as increasing the number of dimensions calls for particular simulation specifications; the dimensionality of such PIC codes imposes limits on both the physical and computational parameter space such as the Debye length, particle size, spacing, and resolution [14]. Utilizing Tristan also has the added advantage of circumventing the normal issues found in employing more traditional non-spectral (local) PIC methods (e.g. resolving the Courant restriction), while also permitting filtering, particle shaping, and resolution control [14].

Tristan, as a relativistic PIC code for plasma physics simulations, self-consistently solves the relativistic equations of motion for charged particles, where the resulting fields are discretized on a finite 3D mesh and time-advanced via the Lorentz force equation in order to ensure second-order accuracy in space and time [15].

2.2 Some necessary Tristan specifics

Tristan (v.2) has some independent dimensionless ‘fiducial’ quantities that are important.

PPC is the number of macroparticles per cell in the PIC code, so that the macroparticle density is $\text{PPC}/\Delta x^3$, and the real density is $n_0 = w_0 \text{PPC}/\Delta x^3$, where w_0 is the number of real particles a macroparticle represents.

C_OMP is the ratio of electron skin depth at density n_0 to Δx , written $\text{C_OMP} = d_e^0/\Delta x$.

σ_0 is the magnetization of a cold plasma with density n_0 in a background magnetic field of $\mathbf{b} = \mathbf{1}$.

$\hat{c} = c \frac{\Delta t}{\Delta x}$ is such that the CFL condition for integrating Maxwell’s equations is $\hat{c} < 1$.

PPC is not of practical interest to us, it’s only important for PIC. C_OMP and \hat{c} don’t affect the physics (which we verified), but they do affect B_{norm} . Obviously \hat{c} is a necessary parameter, it encodes Δt , but so is C_OMP. σ_0 does affect the physics, and additionally affects B_{norm} . The exact relation is $B_{\text{norm}} = \frac{\hat{c}^2 \sqrt{\sigma_0}}{\text{C_OMP}}$.

When Tristan writes electromagnetic fields, it first multiplies them by a factor $\frac{(B_{\text{norm}} C_{\text{OMP}})^2}{2\hat{c}^4 \Delta x^3}$. This can also be written as $\frac{\sigma_0}{2\Delta x^3}$. Δx is implicitly stored in Tristan files, but σ_0 is not. This is why we treat it as a parameter. And this is why \hat{c} and C_{OMP} can't be (and are not) physical parameters. We're not sure where $\frac{\sigma_0}{2\Delta x^3}$ comes from, but it seems to us this σ_0 is just some way to interpret the data. When reading in Tristan data, we make the inverse transformation to obtain \mathbf{e} and \mathbf{b} , which is why we concern ourselves with σ_0 even though it's not explicitly part of the integrators.

We used $\sigma_0 = 10$ throughout, because this gives nicely normalize values of \mathbf{b} and \mathbf{e} , and Tristan (v.2) examples use similar values. We also used $\hat{c} = 0.2$ throughout, because it seems like a nice trade-off between accuracy and speed. (Or it does so for integrating Maxwell's equations anyway.)

2.3 Sampling

For our initial condition, we use particles uniform in space, and just assign \mathbf{u} as a Maxwellian with distribution parameter $a = 1$. Physically this doesn't make much sense, but it's simple. A 1st issue is that \mathbf{u} is not velocity, β is, but these are approximately the same since the initial plasma is relatively cold. A 2nd issue is that it's not Maxwell-Jüttner, but Maxwell-Jüttner is harder to sample. Maxwell-Jüttner would sample \mathbf{u} instead of β . It's harder to sample for two reasons. Firstly, the distribution function is not separable. Secondly, the distribution function is not a simple Gaussian to sample; it must be done some other way, e.g. Monte Carlo. So we're not concerned from simply taking \mathbf{u} as Maxwellian because it's not the right distribution of the snapshot anyway, what we do doesn't differ too much, and is simple. Sampling the electrons uniformly in space is also not physical, and we did write a Monte Carlo sampler to sample according to the electron density of the background field, but didn't use it.

2.4 Boris Mover

We follow the relativistic Boris mover described in [13]. We begin with the *1st half electric of acceleration*

$$\mathbf{u}_1 = \hat{c}\mathbf{u}^{n-1/2} - B_{\text{norm}}\mathbf{e}/2, \quad (8)$$

working in units where $-e/m_e = -1$. Here \mathbf{e} is interpolated from the lattice. We then compute $1/(\hat{c}\gamma) = 1/\sqrt{\hat{c}^2 + \mathbf{u}_1^2}$ and $f = 2/(1 + (B_{\text{norm}}\mathbf{b}/2\hat{c}\gamma)^2)$.² Then follows the *1st half of magnetic acceleration*

$$\mathbf{u}_2 = f(\mathbf{u}_1 - B_{\text{norm}}\mathbf{u}_1 \times \mathbf{b}/2\hat{c}\gamma). \quad (9)$$

Finally there are the *2nd halves of electric and magnetic rotation*

$$\mathbf{u}_3 = \mathbf{u}_1 - B_{\text{norm}}(\mathbf{u}_2 \times \mathbf{b}/2\hat{c}\gamma + \mathbf{e}/2), \quad (10)$$

²This is quite confusing because \mathbf{u} and \mathbf{u}_1 differ by a factor of \hat{c} . It is much simpler to see that $\gamma = \sqrt{1 + \mathbf{u}^2}$, which is obvious because $c\mathbf{u}$ is 3-momentum per mass.

finalizing with $\mathbf{u}^{n+1/2} = \mathbf{u}_3/\hat{c}$. The positions are then updated as $\mathbf{x}^{n+1} = \mathbf{x}^n + \hat{c}\Delta x\beta^{n+1/2}$, where we use the 3-velocity $c\beta^{n+1/2}$.

2.5 Operator Splitting

So far only the Boris mover has been discussed, for relativistically integrating Newton's 2nd law with a Lorentz force. The radiation forces are also velocity dependent, so it would appear we need to redo all the work, coming up with a more complicated mover. But this is not necessary, the operator splitting method described in [16] allows us to continue to use the Boris mover, and implement all 3 forces independently (split). (We generalize the method from 2 to 3 forces.) The idea intuitively is that by using the averaged velocity before and after the previous kick when integrating, the previous kick and current kick are physically applied simultaneously.

Ideally, the leapfrog integrator should look like

$$\frac{\mathbf{p}^{n+1/2} - \mathbf{p}^{n-1/2}}{\Delta t} = \mathbf{F}_L^n + \mathbf{F}_{\text{syn}}^n + \mathbf{F}_{\text{iC}}^n. \quad (11)$$

But all these forces are velocity-dependent, so we don't know them at step n . The method of operator splitting will first solve

$$\frac{\mathbf{p}_L^{n+1/2} - \mathbf{p}^{n-1/2}}{\Delta t} = \mathbf{F}_L^n, \quad (12)$$

using the 2nd order centered mean velocity discussed in Section 1.1. We can show that $\mathbf{p}^{n+1/2} = \mathbf{p}_L^{n+1/2} + (\mathbf{F}_{\text{syn}}^n + \mathbf{F}_{\text{iC}}^n)\Delta t$, which is the basis of operator splitting. We estimate \mathbf{p}^n as $\mathbf{p}_L^n = (\mathbf{p}_L^{n+1/2} + \mathbf{p}^{n-1/2})/2$. We use the \mathbf{p}_L^n estimate to estimate $\mathbf{F}_{\text{syn}}^n$. (Presumably this is 2nd order accurate.) With an explicit estimate of $\mathbf{F}_{\text{syn}}^n$, the integration is no longer implicit. We obtain $\mathbf{p}_{\text{syn}}^{n+1/2}$:

$$\frac{\mathbf{p}_{\text{syn}}^{n+1/2} - \mathbf{p}^{n-1/2}}{\Delta t} = \mathbf{F}_{\text{syn}}^n. \quad (13)$$

$\mathbf{p}_{\text{syn}}^{n+1/2}$ incorporates both \mathbf{F}_L^n and $\mathbf{F}_{\text{syn}}^n$. This simply amounts to $\mathbf{p}_{\text{syn}}^{n+1/2} = \mathbf{p}_L^{n+1/2} + \mathbf{F}_{\text{syn}}^n\Delta t$ practically. We let $\mathbf{p}_{\text{syn}}^{n+1/2}$ estimate \mathbf{p}^n as $\mathbf{p}_{\text{syn}}^n = (\mathbf{p}_{\text{syn}}^{n+1/2} + \mathbf{p}^{n-1/2})/2$. As before, we define

$$\frac{\mathbf{p}_{\text{iC}}^{n+1/2} - \mathbf{p}^{n-1/2}}{\Delta t} = \mathbf{F}_{\text{iC}}^n, \quad (14)$$

where $\mathbf{p}_{\text{syn}}^n$ is used to estimate \mathbf{F}_{iC}^n . This simply amounts to $\mathbf{p}_{\text{iC}}^{n+1/2} = \mathbf{p}_{\text{syn}}^{n+1/2} + \mathbf{F}_{\text{iC}}^n\Delta t$ practically, so $\mathbf{p}^{n+1/2}$ is (estimated by) $\mathbf{p}_{\text{iC}}^{n+1/2}$.

2.6 Parallelization

To obtain good statistical properties of 1D (and especially 2D) histograms, we need hundreds of thousands of particles. It is clear by now that the particles have fully independent

dynamics, i.e. they each evolve independently on the background field. So parallelization is both useful and straight forward. We parallelize by splitting the n particles across multiple threads during every time step. In principle this isn't necessary, the particles are allowed to desynchronize over time, they only have to synchronize when create histograms and such. But if n is large, little is gained by only synchronizing when creating histograms, and synchronizing every timestep is slightly simpler.

3 Results

3.1 Particle Trajectories

Using the 3D turbulence electric and magnetic field data, the dimensions are stored as (z, y, x). The boundary conditions are periodic in all 3 directions. The particles are initialized with a fixed position and velocity and vary for multiple runs. A constant magnetic field is set in the z-direction. The Boris pusher algorithm is then used to update the particle velocity based on the Lorentz force experienced in the electric and magnetic fields. Here electrons are used as the particle species. The velocities for both cooling strengths are kept constant to spot the variation in the 3D plots. Figure 3 and figure 4 depict the particle trajectories of electrons for synchrotron and inverse Compton cooling strengths. As electrons in a plasma emit synchrotron radiation, they lose energy and there will be a decline in their kinetic energy. In the case of inverse Compton cooling, electrons lose energy as they scatter photons, contributing to the cooling of the plasma. When the cooling is weak, particles form a power-law [?].

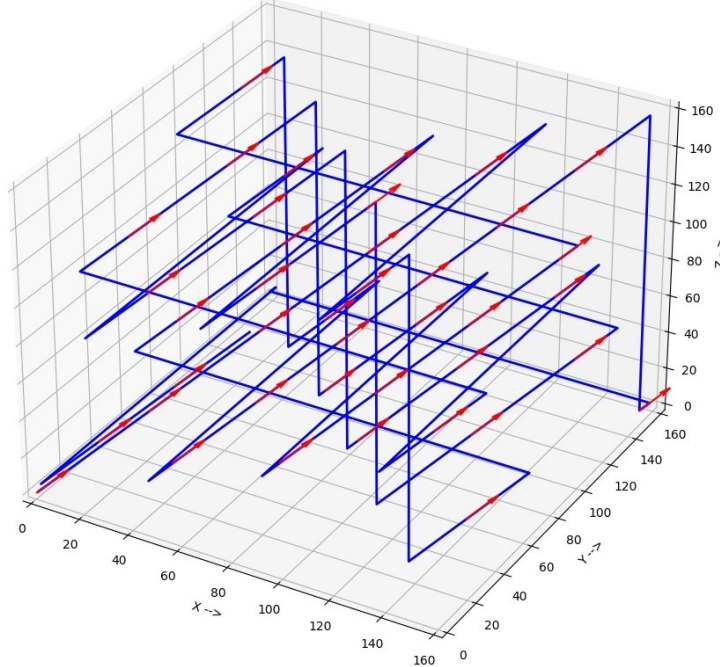


Figure 3: Electron trajectory using synchrotron cooling strength

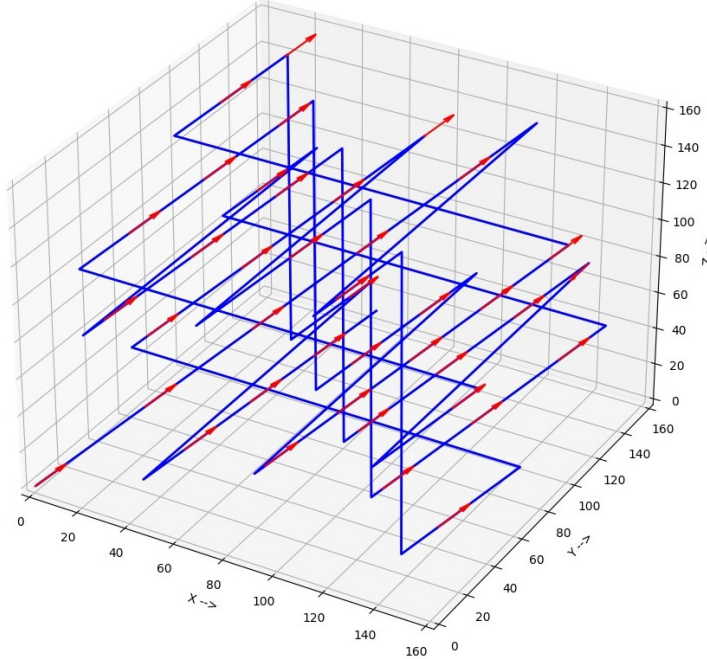


Figure 4: Electron trajectory using inverse Compton cooling strength

3.2 Electron Energy Distribution

All classical relativistic equilibrium electrons have relativistic speeds in a high energy plasma follow the Maxwell-Jüttner distribution, as discussed in earlier sections. The evolution of electron energy distributions for different strengths of synchrotron radiation and inverse Compton cooling can be seen in Figure 5. The peak of energy increases in case of no radiative cooling indicating a significant increase in the kinetic energy of the majority of particles and effective temperature of the plasma (for low γ). Lower values of γ_{ic} and γ_{syn} imply a stronger cooling [1]. We first see an increase, then gradual decrease in kinetic energy and effective temperatures as we go ahead in time for cases where $(\gamma_{\text{ic}}, \gamma_{\text{syn}})$ are (8, 6) and (4, 3), with the decrease of energy being more significant for the later parameters. We can see this by the low γ linear Maxwell-Jüttner regime shifting; shifting upwards is cooling, downwards heating. The panel in the top right where $(\gamma_{\text{ic}}, \gamma_{\text{syn}})$ are (10, 15) shows that, although the kinetic energy is not decreasing with time, the increase in kinetic energy is lower when compared to the case of no radiative cooling.

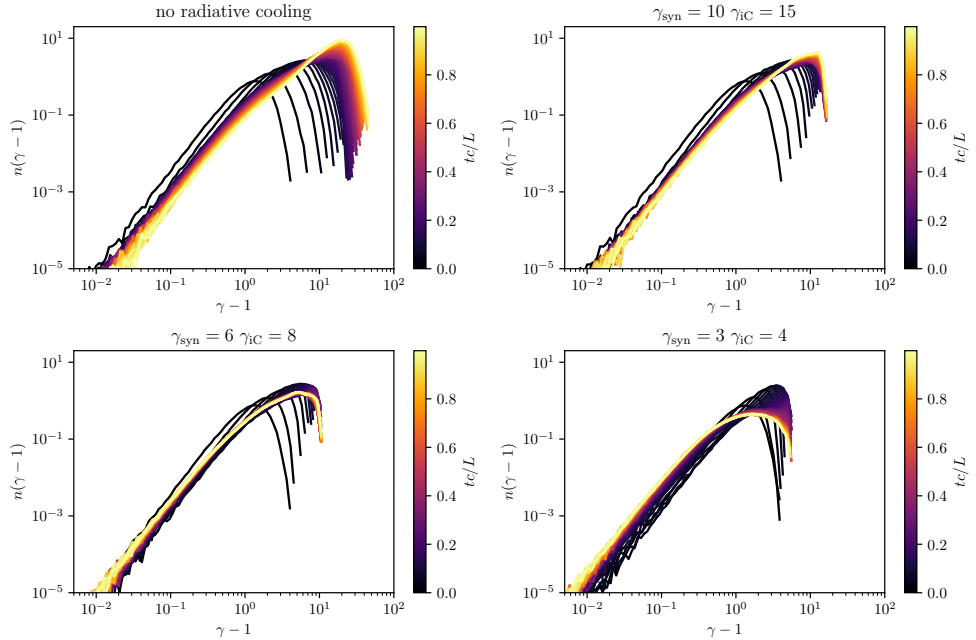


Figure 5: Evolution of electron energy distribution for different cooling strengths

3.3 Steady State Distributions for Different Cooling Strengths

In the steady state regime, we can clearly see the influence of cooling strengths on the electron energy distributions dictated by synchrotron and inverse Compton mechanisms. We can see the effects of these mechanisms when we examine the final energy distributions in Figures 6, 7, and 8.

A Maxwell-Jüttner spectrum is fitted for low γ , and a power law with power c for high γ . Figure 6 has $tc/L = 1.25$, which didn't quite equilibrate, and Figure 7 has $tc/L = 6.25$, which did equilibrate. Figure 6 has slightly nicer fits for c , which increase as cooling strength increases, as expected; cooling introduces a cutoff. But Figure 6 clearly does not equilibrate since the temperature θ is fixed. Figure 7 does show θ decrease with γ_{syn} and γ_{iC} , as expected, due to increased cooling.

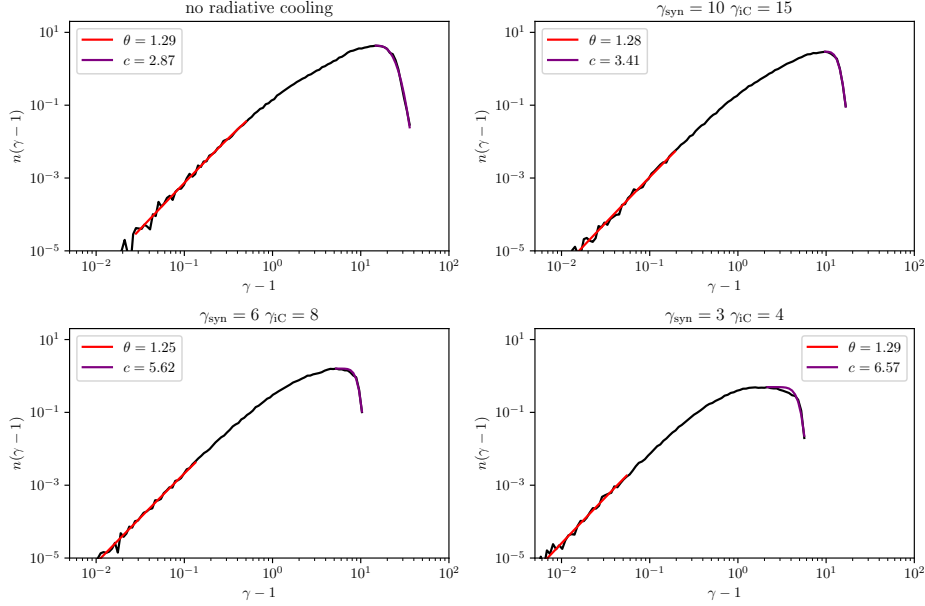


Figure 6: Equilibrium spectra of $n = 10^5$ particles after $N = 10^3$ steps, so $tc/L = 1.25$. Low energy Maxwell-Jüttner spectra and high energy power law behavior are fitted.

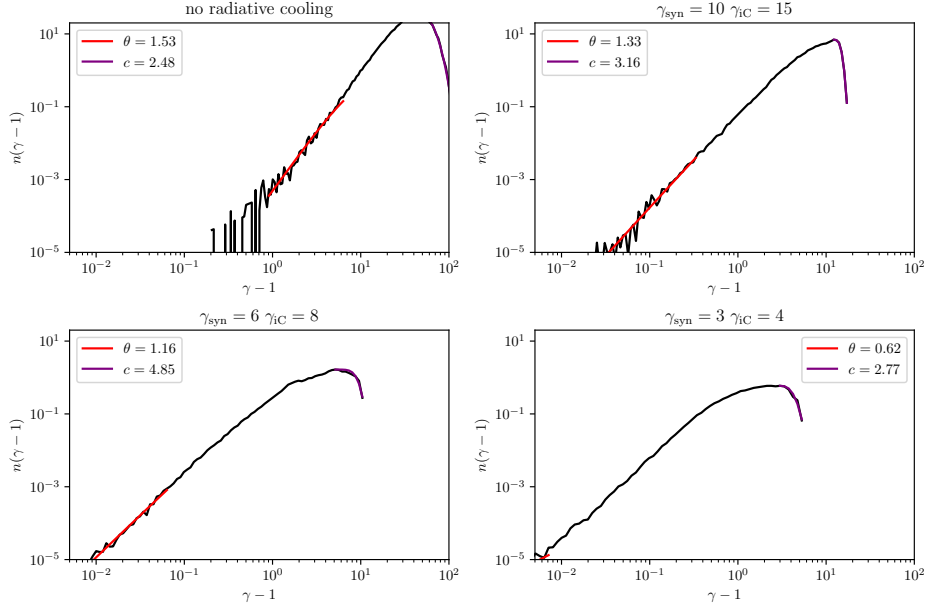


Figure 7: Equilibrium spectra of $n = 10^5$ particles after $N = 5 \times 10^3$ steps, so $tc/L = 6.25$. Low energy Maxwell-Jüttner spectra and high energy power law behavior are fitted.

Next we consider the pitch angle α in Figure 8. For weak cooling conditions ($\gamma_{\text{syn}} = 20$, $\gamma_{iC} = 20$), the electrons retain relatively high energies as indicated by pronounced concentrations around moderate Lorentz factors. As the cooling strength increases ($\gamma_{\text{syn}} = 8$, $\gamma_{iC} = 8$), the distribution broadens and we observe a downward shift in energies which demonstrates the radiative energy losses affecting the plasma. Interestingly when considering

synchrotron cooling in isolation ($\gamma_{\text{syn}} = 8$, $\gamma_{\text{iC}} = \infty$), the distribution mimics the combined cooling scenario, this indicates how the synchrotron effect's shape the particle energy landscape. Whereas, in the scenario dominated by inverse Compton cooling ($\gamma_{\text{syn}} = \infty$, $\gamma_{\text{iC}} = 8$), we notice a substantive spreading in energy distribution, suggesting the different impacts of different cooling processes.

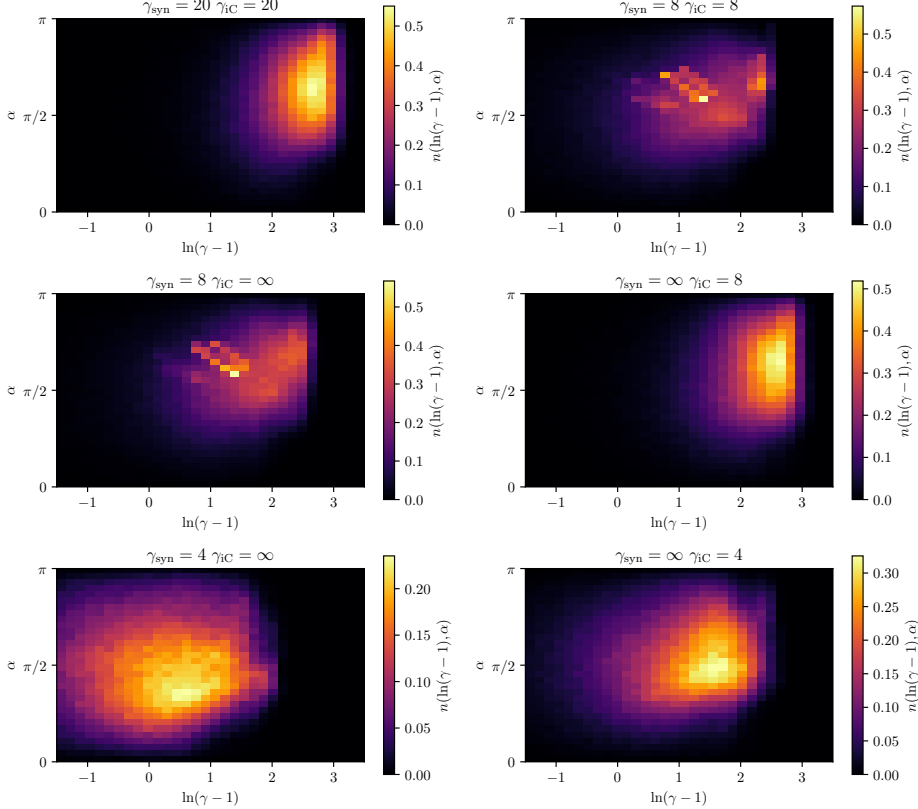


Figure 8: Combined density plots showing the steady-state distribution of pitch angles α function of the Lorentz factor γ under varying synchrotron γ_{syn} and inverse compton γ_{iC} cooling strengths. From left to right, top to bottom, the plots represent scenarios of weak cooling, increased cooling, synchrotron-dominated cooling, and inverse Compton dominated cooling, respectively. The plot reveals how the different radiative cooling mechanisms influence the particle energy distributions within the plasma. This is a simulation of $n = 4 \times 10^5$ particles after $N = 5 \times 10^5$ steps, i.e. $tc/L = 6.25$.

The phase-space plots with strong cooling mechanism ($\gamma_{\text{syn}} = 4$, $\gamma_{\text{iC}} = \infty$ for synchrotron; $\gamma_{\text{syn}} = \infty$, $\gamma_{\text{iC}} = 4$ for inverse Compton) show a stark reduction in energies. We can observe that the distribution reflects a uniformity across various pitch angles which is suggestive of the aggressive energy dissipation due to radiation and isotropy in pitch angle distributions at lower energies.

The line plots in the below figure will further explain these trends, providing a clear picture of the average pitch angle across a spectrum of Lorentz forces.

When we look at the pitch angle α distributions, our analysis unveils distinct distributions

occurring on the electron energy E_e and the prevalent cooling processes as shown in Figure 9. The pitch angle is indicative of the directional alignment between the electron velocity and the magnetic field which offers a window into the anisotropy belonging to the plasma dynamics under varying cooling influences. We have a slight \mathbf{B} column along $\hat{\mathbf{z}}$. The structure we see for ($\gamma_{\text{syn}} = 8$, $\gamma_{\text{iC}} = \infty$) is presumably precession of the electrons ($q < 0$), moving towards $-\hat{\mathbf{z}}$ ($\alpha > \pi/2$), which we postulate because by comparing Figure 9 to Figure 8, it's clear there's more alignment, in particular for highly relativistic electrons.

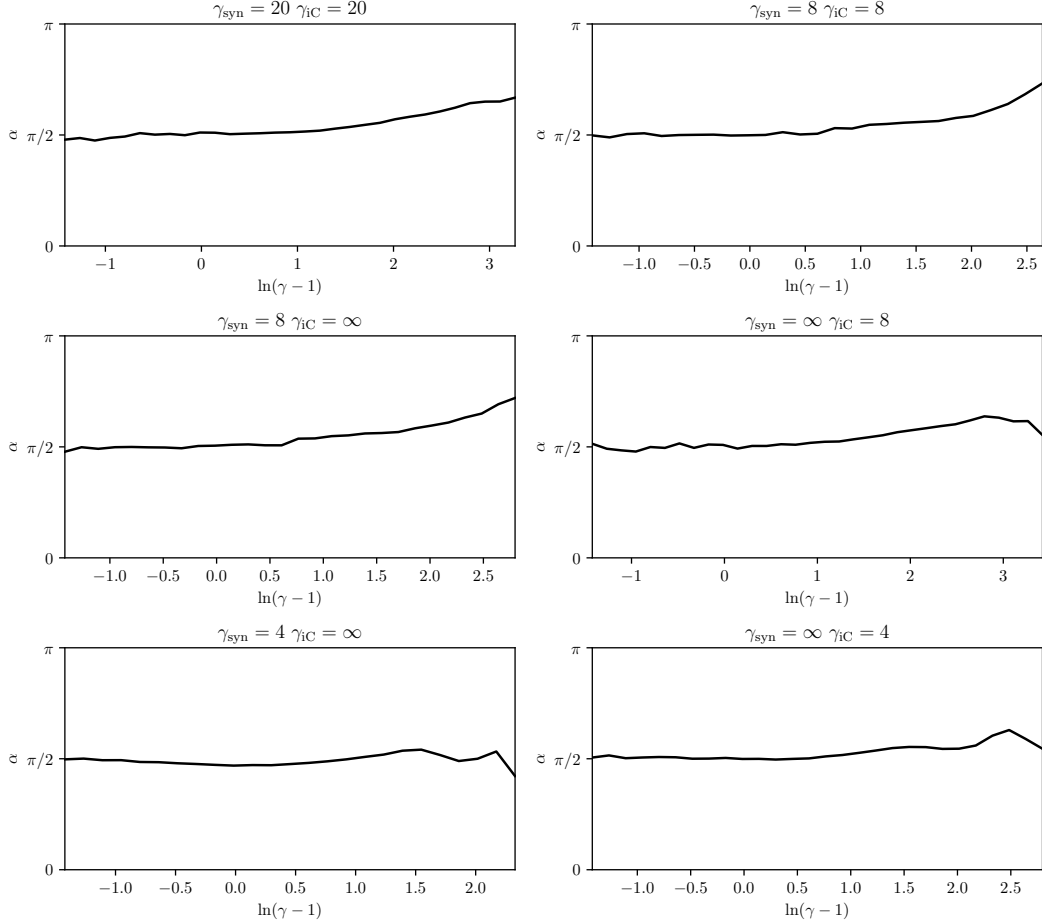


Figure 9: Pitch angle distributions vs. Lorentz factor (γ) illustrating the effects of variable cooling regimes. Plots demonstrate scenarios with weak (Top left: $\gamma_{\text{syn}} = 20, \gamma_{\text{iC}} = 20$), moderate (Top right: $\gamma_{\text{syn}} = 8, \gamma_{\text{iC}} = 8$), strong synchrotron (Middle left: $\gamma_{\text{syn}} = 8, \gamma_{\text{iC}} = \infty$), strong inverse Compton (Middle right: $\gamma_{\text{syn}} = \infty, \gamma_{\text{iC}} = 8$), and extreme cooling cases for synchrotron (Bottom left: $\gamma_{\text{syn}} = 4, \gamma_{\text{iC}} = \infty$) and inverse Compton (Bottom right: $\gamma_{\text{syn}} = \infty, \gamma_{\text{iC}} = 4$). Each plot reveals how radiative cooling influences electron pitch angle anisotropy within the plasma. This is a simulation of $n = 4 \times 10^5$ particles after $N = 5 \times 10^5$ steps, i.e. $tc/L = 6.25$; same simulation as Figure 8.

In the absence of strong cooling ($\gamma_{\text{syn}} = 20, \gamma_{\text{iC}} = 20$), the distribution maintains a median pitch angle around $\alpha = \frac{\pi}{2}$ which suggests an even spread between parallel and anti-parallel alignments with the magnetic field. As cooling becomes more effective ($\gamma_{\text{syn}} = 8, \gamma_{\text{iC}} = 8$) the distribution widens, indicating at an increased perturbation in particle trajectories due

to more significant energy losses.

The plots centred around synchrotron cooling show a homogeneous pitch angle distribution across different energy states, which essentially confirms the magnetic field's role in influencing the electron motion. On the contrary, the inverse-Compton dominated scenario presents a different pitch-angle distribution which highlights a divergence from magnetic field aligned movements.

In scenarios of intensive radiative cooling, the distributions become more isotropic, with no clear preference for particular pitch angles. This finding suggests that at lower energies, induced by substantial cooling, the electrons have more randomized motion, diverging from the magnetic field lines.

In comparing strong synchrotron cooling with strong inverse Compton cooling, we observe that synchrotron cooling gives rise to a more uniform pitch angle distribution across the energy spectrum, whereas inverse Compton cooling results in a more subtle distributions, especially at higher energies. It is apparent that the nature of cooling mechanisms deeply impact the angular distribution of velocities concerning the magnetic field, which yielded us useful insights into the energy dissipation and particle acceleration processes.

3.4 Transferred Power

As is well known, magnetic fields transfer no power, because the magnetic component of the Lorentz force is perpendicular to \mathbf{v} . The electric field does transfer power. Let \mathbf{E}_{\parallel} and \mathbf{E}_{\perp} be the components of $\mathbf{E} = B_{\text{norm}}\mathbf{e}$ parallel and perpendicular to $\mathbf{B} = B_{\text{norm}}\mathbf{b}$ respectively, i.e. $\mathbf{E}_{\parallel} = \frac{\mathbf{E} \cdot \mathbf{B}}{\mathbf{B} \cdot \mathbf{B}} \mathbf{B}$ and $\mathbf{E}_{\perp} = \mathbf{E} - \mathbf{E}_{\parallel}$. The power transferred is $P_{\parallel} = -e\mathbf{v} \cdot \mathbf{E}_{\parallel}$ and $P_{\perp} = -e\mathbf{v} \cdot \mathbf{E}_{\perp}$. We are interested in P_{\parallel}/P_{\perp} . Figures 10 to 13 shows time dependent histograms over various durations tc/L . Clearly most power comes from P_{\perp} , across all time scales. We see in Figure 10 that, especially early on, and especially for relativistic particles, γ_{\perp} dominates. Later on (but still before equilibration), as seen in 12, the spectrum is flatter. In Figure 13, we see that for high cooling (bottom right), P_{\perp} increases with γ . Overall it's a complicated evolution, and this still hasn't equilibrated fully; these simulations take hours.

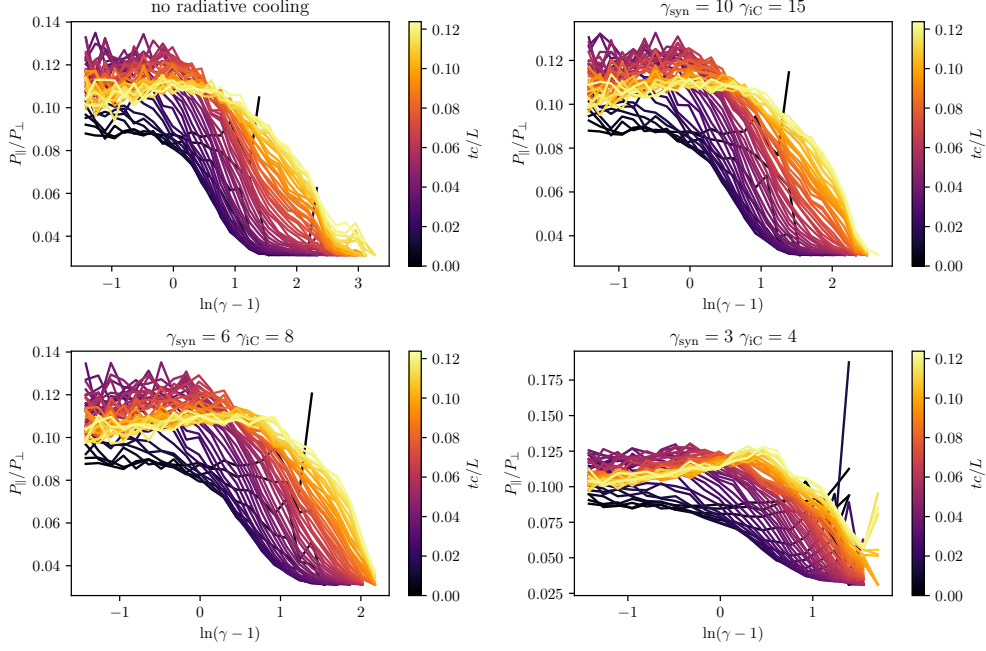


Figure 10: P_{\parallel}/P_{\perp} for $n = 4 \times 10^5$ particles with duration $tc/L = 0.125$, or $N = 100$ steps.

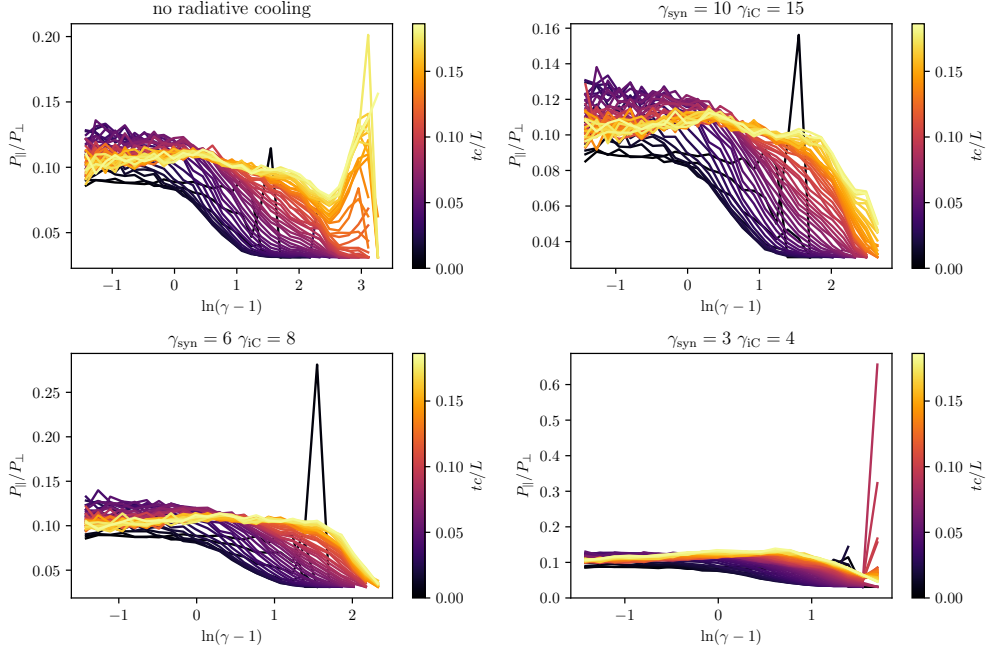


Figure 11: P_{\parallel}/P_{\perp} for $n = 4 \times 10^5$ particles with duration $tc/L = 0.188$, or $N = 150$ steps.

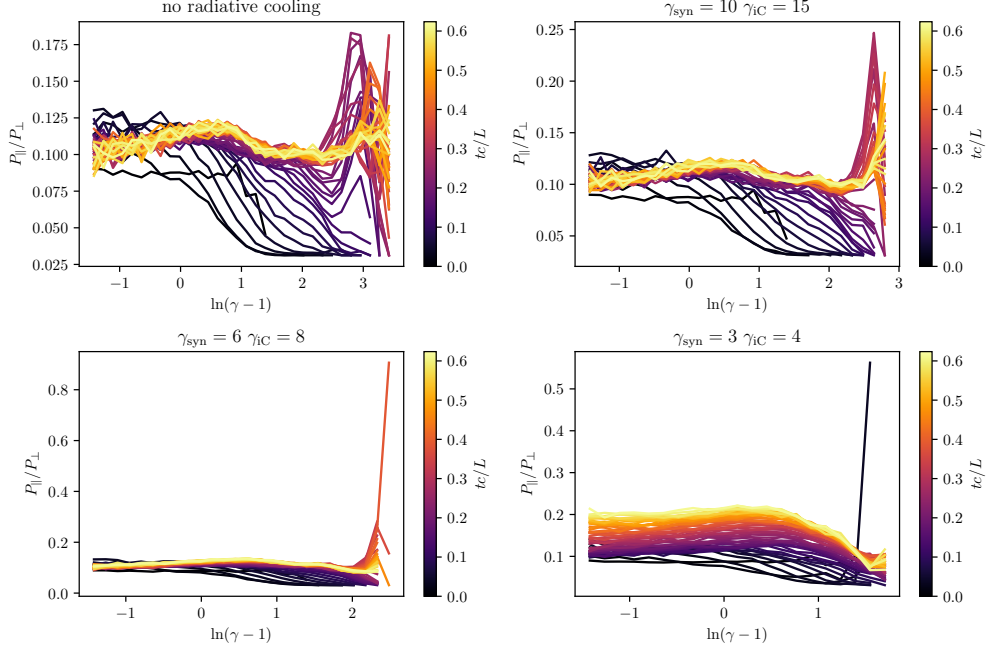


Figure 12: P_{\parallel}/P_{\perp} for $n = 4 \times 10^5$ particles with duration $tc/L = 0.625$, or $N = 500$ steps.

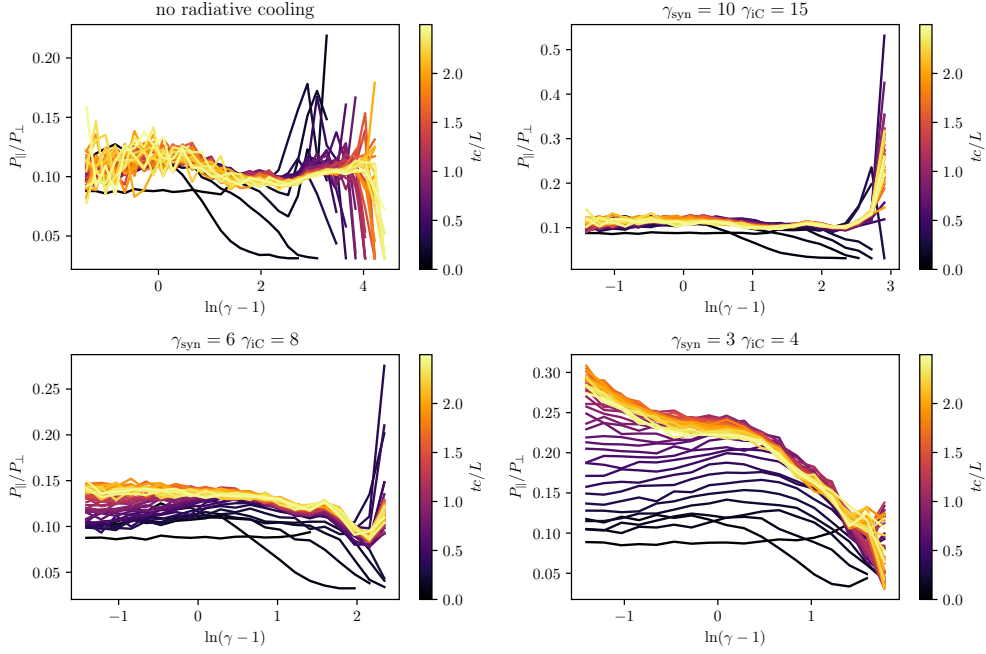


Figure 13: P_{\parallel}/P_{\perp} for $n = 4 \times 10^5$ particles with duration $tc/L = 2.5$, or $N = 2000$ steps.

4 Conclusion

We have demonstrated the use of the operator splitting method to numerically integrate the motion of a particle in a 3D periodic turbulent box with synchrotron radiation and inverse Compton cooling. We observe that the evolution of electron energy distribution depends on the inverse Compton cooling (γ_{IC}) and synchrotron radiation (γ_{syn}) strengths. Weaker cooling implies there is a substantial rise in kinetic energy and effective temperature over time, indicating minimal radiative cooling effects. The influence of radiative energy losses on the plasma is seen as the broadening of the distribution (but with a power law cutoff) and a decline in energies as cooling strength rises. It was noted that even in isolation, synchrotron cooling reproduces the case of combined cooling, demonstrating its important influence on particle energy landscapes. Pitch angle distribution analysis gave a glimpse of the anisotropic nature of plasma dynamics under different cooling conditions due to the (slight) \mathbf{B} column along $\hat{\mathbf{z}}$. The behavior is generally complicated, producing more structure, interpreted as clear precession, for certain cooling parameters that are neither too small nor too large. Finally, we found that most power transfer to the electron (feeding the radiative cooling) comes from \mathbf{E}_{\perp} , again with overall complicated γ and time dependence.

References

- [1] Daniel Groselj, Hayk Hakobyan, Andrei M. Beloborodov, Lorenzo Sironi, and Alexander Philippov. Ab initio turbulent comptonization in magnetized coronae of accreting black holes, 2023.
- [2] D A Uzdensky. Relativistic turbulence with strong synchrotron and synchrotron self-Compton cooling. *Monthly Notices of the Royal Astronomical Society*, 477(3):2849–2857, 03 2018.
- [3] Vladimir Zhdankin, Dmitri A. Uzdensky, and Matthew W. Kunz. Production and Persistence of Extreme Two-temperature Plasmas in Radiative Relativistic Turbulence. , 908(1):71, February 2021.
- [4] N. S. Kardashev. Nonstationarity of Spectra of Young Sources of Nonthermal Radio Emission. , 6:317, December 1962.
- [5] R. Schlickeiser. A viable mechanism to establish relativistic thermal particle distribution functions in cosmic sources. , 143:431–434, February 1985.
- [6] Jonathan Mackey, Thomas A K Jones, Robert Brose, Luca Grassitelli, Brian Reville, and Arun Mathew. Inverse-compton cooling of thermal plasma in colliding-wind binaries. *Monthly Notices of the Royal Astronomical Society*, 526(2):3099–3114, September 2023.
- [7] Vlad Muşat, Andrea Latina, and Gerardo D’Auria. A high-energy and high-intensity inverse compton scattering source based on compactlight technology. *Photonics*, 9(5), 2022.
- [8] J. Michael Burgess, Damien Bégué, Jochen Greiner, Dimitrios Giannios, Ana Bacelj, and Francesco Berlato. Gamma-ray bursts as cool synchrotron sources. *Nature Astronomy*, 4(2):174–179, October 2019.
- [9] Alexander Chernoglazov, Hayk Hakobyan, and Alexander A. Philippov. High-energy radiation and ion acceleration in three-dimensional relativistic magnetic reconnection with strong synchrotron cooling, 2023.
- [10] J.L. Synge. *The Relativistic Gas, By J.L. Synge.* Series in Physics. North-Holland, 1957.
- [11] A. Kertanguy. Relativistic corrections to the maxwellian distribution for astrophysical and fusion plasmas. *Journal of Applied Mathematics and Physics*, 11:2414–2428, 01 2023.
- [12] Lorenzo Zaninetti. New probability distributions in astrophysics: Iv. the relativistic maxwell-boltzmann distribution. *International Journal of Astronomy and Astrophysics*, 2020.

- [13] J. Nättilä. Runko: Modern multiphysics toolbox for plasma simulations. *Astronomy and Astrophysics*, 664:A68, August 2022.
- [14] O. Buneman, C.W. Barnes, J.C. Green, and D.E. Nielsen. Principles and capabilities of 3-d, e-m particle simulations. *Journal of Computational Physics*, 38(1):1–44, 1980.
- [15] Anatoly Spitkovsky, Luis Gargate, Jaehong Park, and Lorenzo Sironi. TRISTAN-MP: TRIdimensional STANford - Massively Parallel code. Astrophysics Source Code Library, record ascl:1908.008, August 2019.
- [16] M Tamburini, F Pegoraro, A Di Piazza, C H Keitel, and A Macchi. Radiation reaction effects on radiation pressure acceleration. *New Journal of Physics*, 12(12):123005, December 2010.

Appendix

Code: [Github link](#)